Power Coupling Index (PCI) Oriented Stability Analysis and Interaction Control Design for Inverter-Based Microgrid Under Complex Line Impedance

Siqi Fu, Yao Sun, *Member, IEEE*, Xiaochao Hou, *Member, IEEE*, Feng Zhou, Mei Su, Xin Zhang, *Senior Member, IEEE*, and Kai Sun, *Fellow, IEEE*

***Abstract*—In the distributed power grid with renewable power generation that works based on converters, the grid-forming inverter is a crucial component. Under different line impedance, a given control-based inverter would be instability due to the complex power coupling. Thus, it is necessary to study the inverter operation boundary and the control rule by fully considering the quantitative power coupling. In this article, a power coupling index (PCI) oriented stability analysis and [P Q]-[ω V] interactive control design for inverter-based microgrid is comprehensively studied. First, a unified inverter control framework is introduced to work under any type of network impedance. Then, a generalized PCI is constructed based on relative gain array analysis method to characterize the degree of power coupling, which facilitates interpretation of the general adaptability of the proposed control method. Meanwhile, the mechanism of power coupling and system stability under different line X/R ratio are analyzed, and interestingly, it is found that the design rules of control parameters between highly-inductive and highly-resistive line impedances are totally inverse. Finally, the comparative experiments verify the results of PCI-oriented stability analysis and the proposed universal control.**

***Index Terms*—Grid-forming inverter, microgrid, renewable power generation.**

Received 22 May 2024; revised 17 August 2024 and 12 October 2024; accepted 21 October 2024. Date of publication 28 October 2024; date of current version 18 December 2024. This work was supported in part by the National Natural Science Foundation of China under Grant 62125308, Grant 52337008, and Grant 52377168, in part by the Hunan Provincial Natural Science Foundation of China under Grant 2024JJ4055, and in part by the State Key Laboratory of Power System Operation and Control under Grant SKLD23KM12. Recommended for publication by Associate Editor A. Gupta. *(Corresponding author: Feng Zhou.)*

Siqi Fu and Feng Zhou are with the College of Electronic Information and Electrical Engineering, Changsha University, Changsha 410082, China (e-mail: z20240836@ccsu.edu.cn; zhoufeng@ccsu.edu.cn).

Yao Sun and Mei Su are with the School of Automation, Hunan Provincial Key Laboratory of Power Electronics Equipment and Gird, Central South University, Changsha 410083, China (e-mail: yaosun@csu.edu.cn; sumeicsu@csu.edu.cn).

Xiaochao Hou is with the School of Electronic Information, Central South University, Changsha 410004, China (e-mail: houxc10@csu.edu.cn).

Xin Zhang is with the College of Electrical Engineering, Zhejiang University, Hangzhou 310027, China (e-mail: zhangxin_ieee@163.com).

Kai Sun is with the State Key Laboratory of Power System Operation and Control, Department of Electrical Engineering, Tsinghua University, Beijing 100084, China (e-mail: sunkai@tsinghua.edu.cn).

Color versions of one or more figures in this article are available at https://doi.org/10.1109/TPEL.2024.3487394.

Digital Object Identifier 10.1109/TPEL.2024.3487394

I. Introduction

BECAUSE of the fast decarbonization of power systems, renewable energy generation gradually replaces synchronous generator generation [1], [2]. Renewable energy usually transmits energy to the grid through converters, which generally operate in grid-following and grid-forming mode. The grid-following converter does not have the ability to work in the island mode, and it is prone to instability when connected to the weak power grid. Grid-forming converters provides frequency/voltage support that increases the permeation of converters in the power grid. Besides, poorly designed grid-forming converters might be detrimental to system stability [3].

The basic control of grid-forming converters is droop control that generates angle and amplitude [4], [5] that achieves power sharing and frequency/voltage regulation. Under different line impedance, the coupling relationship of [P Q]-[ω V] is complex, and many researches of control design have been studied.

A. Background Description

The distributed power interface is usually configured with *LC* or *LCL* filters, and some power supplies require transformers for voltage boost. The existence of filters and transformers makes the line impedance mostly appear inductive [6]. However, when the line inductance is large and the resistance is small, the system is easy to suffer medium-frequency (tens of Hz) power oscillation [7], [8], [9], [10]. Besides, for rural low-voltage ac microgrids, the main line characteristic is resistive. Q-ω boost control [11] is adapted to this scenario, but it is not compatible with the power grid, which uses active power to adjust frequency. However, P-ω droop control with mismatched droop parameters will cause poor dynamic performance. After medium voltage transmission, the line impedance is generally complex resistive-inductive. The traditional decoupling control helps ensure the system stability, but it can not fully realize the decoupling and parameter design is difficult. The classical control laws under the above different line impedances are summarized in Table I. It is worth noting that the grid-forming control operating algorithms of inverter manufacturers are not always applicable for the all scenarios, as shown in Fig. 1. It inspires us to study unified

TABLE I
DROOP RELATIONS UNDER DIFFERENT LINE IMPEDANCE

Types of line	P-Q Relations	Droop Laws
L $\theta \approx 90$	$P \approx V_g V_i \delta / X$ $Q \approx V_g (V_i - V_g) / X$	$\omega = \omega_n - m_p P$ $V_i = V_n - n_q Q$
RL $\theta \approx 45$	$P - Q \approx \sqrt{2} V_g V_i \delta / Z$ $P + Q \approx \sqrt{2} V_g (V_i - V_g) / Z$	$\omega = \omega_n - m(P - Q)$ $V_i = V_n - n(P + Q)$
R $\theta \approx 0$	$P \approx V_g (V_i - V_g) / R$ $Q \approx -V_g V_i \delta / R$	$\omega = \omega_n + m_q Q$ $V_i = V_n - n_p P$

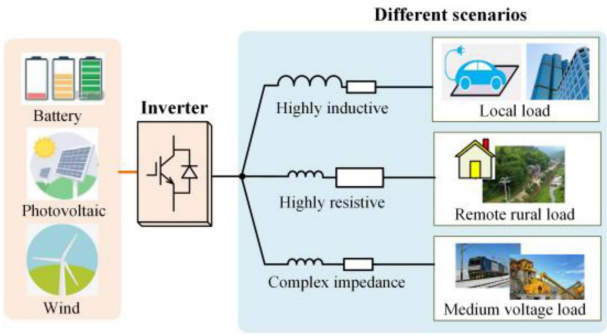

Fig. 1. Schematic diagram of scenarios under different types of line impedances.

analysis methods to analyze the influence rules of parameters and universal control method of different scenarios.

B. Literature Review

To get rid of the dependence on line impedance, the main method is the virtual impedance technique. When the line impedance is highly inductive, considering the dynamics of line inductance, medium-frequency power oscillation exists, which may cause system instability [7], [8], [9], [10]. Connecting a real resistor to the converter can suppress the medium-frequency power oscillation, but produces additional loss. Thus, a virtual resistance is applied in [9]. When the line impedance is complex resistive-inductive or highly resistive, virtual inductance [12], [13], and virtual negative reactance [14], which changes the resistance-inductance ratio of the impedance, are employed to help power decoupling. Rodriguez-Cabero et al. [12] put forward a design standard for virtual impedance to cope with a wide range of impedance changes. Wen et al. [13] calculated the optimal value of virtual inductance and reveals the physical interpretation of power decoupling. As an alternative, He and Li [14] introduced a virtual negative resistor technique. As a result, the inductive nature of the line impedance increases, and there is less power coupling. However, after applying the virtual negative resistor technique, the stability margins of the inverter are significantly impacted and reduced.

In addition to the virtual impedance method, De Brabandere et al. [15] early innovatively proposed a virtual power control strategy by introducing a transformation matrix related to line impedance, which achieves the modified power-sharing. It provides a new perspective for later research, and the essence of the method is to eliminate the power coupling of the control loop. Furthermore, the core idea of control in literature [16], [17] comes from [15], and virtual frequency and virtual voltage are introduced by means of a transformation matrix to realize power decoupling. Besides, Yan and Zhang [18] and Zhang and Raheja [19] designed cross feed forward control of frequency and voltage to help the power decoupling. Furthermore, Chen et al. [20] discussed structures of the modified grid-forming control, design the grid-forming converter through multi-input and multioutput ways. Furthermore, Rathnayake and Bahrani [21] and Chen et al. [22] proposed multivariable feedback controls of the grid forming converter and employs H∞-based methods to adjust the control parameters. Chen et al. [23] proposed a full-state feedback control scheme and step-by-step pole placement-based parameter design approach.

C. Work Motivation

In a word, the adaptation mechanism of the aforementioned control methods is unclear under complex line impedance, and the influence of control parameters on the degree of power coupling is not analyzed. Specifically, it does not provide the control rule by fully considering the quantitative power coupling for a given grid-forming inverter under three different types of (highly inductive, highly resistive, and complex resistive-inductive) line impedances.

Hence, this article conducts power coupling index (PCI) oriented stability analysis and control design for inverter-based microgrid under complex line impedance. The contributions of the article can be summarized as follows.

1) A [P Q]-[ω V] interactive control framework is introduced that unify the different grid-forming control by studying the dynamic control law of the virtual impedance from the perspective of the nodal amplitude-phase characteristics, which is enabled to work under any type of network impedance by appropriate control design. Moreover, compared with virtual impedance, the proposed control framework possesses more independent control freedom.
2) A generalized PCI is constructed based on relative gain array analysis method to characterize the degree of power coupling. The power coupling of [P Q]-[ω V] always exists under arbitrary line R/X ratio, and thus, this article quantitatively analyzes the influence of power coupling and makes use of it to guide parameter design.
3) The design rules of universal droop control parameters under highly-inductive and highly-resistive line impedances are inverse due to the different mechanism of power coupling. Under highly inductive line impedance, *P-V* droop coefficient n_x and *Q-δ* feedback coefficient m_x dominate the system stability and the degree of power coupling in medium frequency band. Increasing n_x and m_x effectively suppress the medium frequency oscillation. Conversely, under highly resistive line impedance, decreasing n_x and m_x, and increasing the *Q-V* droop coefficient n_d can decrease the degree of power coupling in low frequency band and speed up the adjusting time.

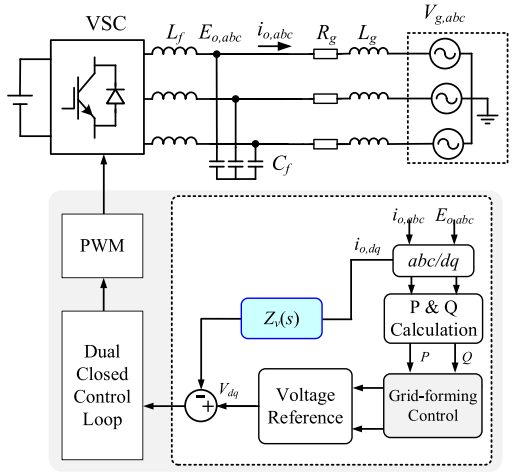

Fig. 2. Basic control block diagram including virtual impedance.

II. [*P Q*]-[ωV] Interactive Control Framework of Inverter-Based Microgrid

There are two kinds of classical droop control methods under different line impedances. One is *P*-ω droop control under highly inductive line impedance to achieve active power sharing. The other is *Q*-ω droop control under highly resistive line impedance to achieve reactive power sharing. The form and function of them are not uniform. In this section, we try to unify an inverter control framework that is enabled to work under any type of network impedance, and then give a comprehensive stability analysis and control design based on the [P Q]-[ω V] interactive framework in the subsequent section.

Fig. 2 shows the basic control block diagram of a grid-forming converter including the virtual impedance, where the bandwidth of the dual closed loop is assumed to be much larger than that of the power control. Thus, ignoring the dual closed loop, and the virtual impedance can be expressed as

$$\tilde{\vec{E}}_{o,dq} = \tilde{\vec{V}}_{r,dq} - \tilde{\vec{i}}_{o,dq} Z_v(s) \tag{1}$$

where $\vec{E}_{o,dq}$, $\vec{V}_{dq}$, and $\vec{i}_{o,dq}$ represents, respectively, the vectors of output voltage, voltage reference, and output current in *dq* synchronous frame, ~ is the small variations in variables, and $\hat{\vec{x}}_{dq} = \hat{x}_d + j\hat{x}_q$. Aligning the steady phase angle δ_n with axis *d*, after *dq* transformation, $E_{o,d} = E_o \cos\delta_{\text{on}}$, $E_{o,q} = E_o \sin\delta_{\text{on}}$, $V_{r,d} = V_r \cos\delta_{rn}$, and $V_{r,q} = V_r \sin\delta_{rn}$. $\delta_{\text{on}} = \delta_o - \delta_n$ and $\delta_{rn} = \delta_r - \delta_n$. δ_r and δ_o are the angles of voltage reference and output voltage, respectively. Virtual resistance and steady-state inductance $Z_v = R_v + jX_v$ are taken as a typical example to derive the equivalent power characteristics of virtual impedance.

The phasor diagram of voltage and current is drew, as shown in Fig. 3, where $\delta_{ro} = \delta_r - \delta_o$. The output power can be expressed as

$$\begin{cases} P = \frac{1.5}{{R_v}^2+{X_v}^2}\left(R_v {V_r}^2 - R_v V_r E_o \cos\delta_{ro} + X_v V_r E_o \sin\delta_{ro}\right) \\ Q = \frac{1.5}{{R_v}^2+{X_v}^2}\left(X_v {V_r}^2 - X_v V_r E_o \cos\delta_{ro} - R_v V_r E_o \sin\delta_{ro}\right). \end{cases} \tag{2}$$

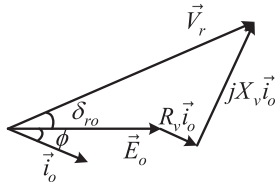

Fig. 3. Phasor diagram of voltage and current.

Linearizing the output power around equilibrium points yields

$$\begin{cases} \tilde{P} = \frac{1.5}{{R_v}^2+{X_v}^2}\left[X_v E_{o0} V_{r0}\left(\tilde{\delta}_r - \tilde{\delta}_o\right) - R_v E_{o0}\tilde{E}_o \right. \\ \qquad \left. + R_v\left(2V_{r0} - E_{o0}\right)\tilde{V}_r\right] \\ \tilde{Q} = \frac{1.5}{{R_v}^2+{X_v}^2}\left[-R_v E_{o0} V_{r0}\left(\tilde{\delta}_r - \tilde{\delta}_o\right) + X_v(2V_{r0} \right. \\ \qquad \left. - E_{o0})\tilde{V}_r - XV_{r0}\tilde{E}_o\right] \end{cases} \tag{3}$$

where the subscript suffix "$_0$" stands for the steady-state value. The phase difference between nodes is usually small, assuming $\sin\delta_{or0} \approx 0$ and $\cos\delta_{or0} \approx 1$ where $\delta_{or0} = \delta_{o0} - \delta_{r0}$, i.e., the steady-state angle difference of output voltage and reference voltage.

In addition, the voltage amplitude sag is assumed to be small, i.e., $E_{o0} \approx V_{r0}$. The following relationship can be obtained:

$$\begin{cases} \tilde{V}_r - \tilde{E}_o = \frac{2}{3} \cdot \frac{R_v\tilde{P} + X_v\tilde{Q}}{V_{r0}} \\ \tilde{\delta}_r - \tilde{\delta}_o = \frac{2}{3} \cdot \frac{X_v\tilde{P} - R_v\tilde{Q}}{E_{o0}V_{r0}}. \end{cases} \tag{4}$$

Furthermore, replacing E_{o0} and V_{r0} with voltage reference V^* since the voltage amplitude is limited to the allowable range. Thus, the virtual inductance control can be equivalent to

$$\begin{cases} \delta_o = \delta_r - \frac{X_v}{V^{*2}}P \\ E_o = V_r - \frac{X_v}{V^*}Q. \end{cases} \tag{5}$$

The classical virtual resistance control can be equivalent to

$$\begin{cases} \delta_o = \delta_r + \frac{R_v}{V^{*2}}Q \\ E_o = V_r - \frac{R_v}{V^*}P. \end{cases} \tag{6}$$

Similarly, any form of virtual impedance $Z_v(s)$ can be represented based on (5) and (6). To get rid of the dependence on line impedance, the main and common method is the virtual impedance technique on the basis of classic droop control, which has been verified by the existing research work [6], [12], [13], [14]. Therefore, combining (5) and (6), the unified interactive control framework the control method under the [P Q]-[ω V] framework of parallel inverter can be expressed as

$$\begin{cases} \omega = \omega^* - m\left(P - P^*\right) \\ \delta_o = \int \omega\, dt - m_d P + m_x Q \\ E_o = V^* - n_d\left(Q - Q^*\right) - n_x P \end{cases} \tag{7}$$

where *m,* n_d, and m_d represent the *P*-ω, *Q*-*V,* and the *P*-δ droop coefficient, respectively. Importantly, n_x and m_x represent the coupling *P*-*V* droop coefficient and the coupling *Q*-δ feedback coefficient, respectively. ω^*, P^*, and Q^* are the nominal angular frequency, reference of active power and reactive power.

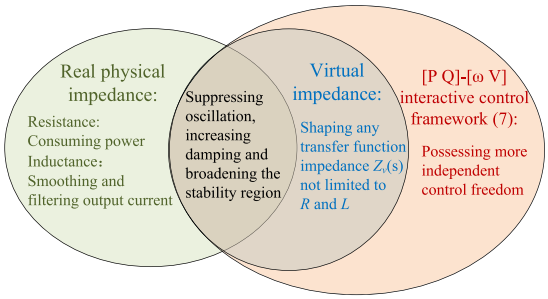

Fig. 4. Correlation diagram among real impedance, virtual impedance, and [P Q]-[ω V] interactive control framework.

Furthermore, the correlation diagram among real impedance, virtual impedance and [P Q]-[ω V] interactive control framework is concluded as Fig. 4 shows. All help suppress oscillations, increasing damping and broadening the system stability region. Besides, real resistance consumes power and real inductance helps smooth and filter output current. Virtual impedance control shapes transfer function impedance Z_v(s) not limited to R and L, which the power feedback control can do. Moreover, [P Q]-[ω V] interactive control framework possesses more independent control freedom.

It is worth noting that the unified [P Q]-[ω V] interactive control framework is inherently a universal droop control type. It makes the converter adapt to any type of line impedance and ensures frequency synchronization between multiple inverters without affecting the accurate active power sharing. The parameter m_d, n_d, m_x, and n_x can also be designed freely and flexibly to provide more independent freedom for the system, which would be discussed in the following section.

III. PCI-Oriented Stability Analysis

In this section, the system small signal model is established and a generalized characterization index is constructed to characterize the degree of power coupling. Furthermore, PCI-oriented stability under different line impedances is analyzed.

A. Small Signal Model

According to Fig. 1, the line inductance dynamic model in the small signal is expressed as

$$\begin{cases} L_g \frac{d\tilde{i}_{o,d}}{dt} = \tilde{E}_{o,d} - \tilde{V}_{gd} - \tilde{i}_{o,d} R_g + \omega_n L_g \tilde{i}_{o,q} \\ L_g \frac{d\tilde{i}_{o,q}}{dt} = \tilde{E}_{o,q} - \tilde{V}_{gq} - \tilde{i}_{o,q} R_g - \omega_n L_g \tilde{i}_{o,d} \end{cases} \tag{8}$$

where R_g and L_g represent line resistance and line inductance, $V_{gd} = V_g \cos\delta_{gn}$, $V_{gq} = V_g \sin\delta_{gn}$, and V_g represent grid voltage amplitude.

Linearizing output power around equilibrium points yields

$$\begin{cases} \tilde{P} = 1.5\left(\tilde{E}_{o,d} i_{o,d0} + E_{o,d0}\tilde{i}_{o,d} + \tilde{E}_{o,q} i_{o,q0} + E_{o,q0}\tilde{i}_{o,q}\right) \\ \tilde{Q} = 1.5\left(-\tilde{E}_{o,d} i_{o,q0} - E_{o,d0}\tilde{i}_{o,q} + \tilde{E}_{o,q} i_{o,d0} + E_{o,q0}\tilde{i}_{o,d}\right). \end{cases} \tag{9}$$

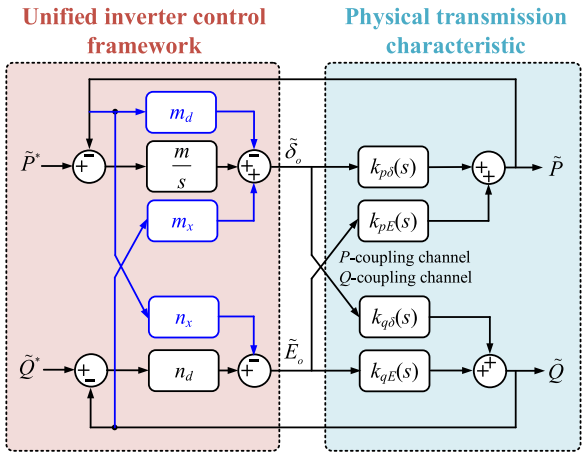

Fig. 5. Closed-loop small-signal block diagram of the system.

Calculating the output power combining (8) and (9) yields

$$\begin{aligned} \tilde{P} &= k_{p\delta}(s)\,\tilde{\delta}_o + k_{pE}(s)\,\tilde{E}_o \\ \tilde{Q} &= k_{q\delta}(s)\,\tilde{\delta}_o + k_{qE}(s)\,\tilde{E}_o \end{aligned} \tag{10}$$

where

$$\begin{cases} k_{p\delta}(s) = \frac{{E_{o0}}^2 X_g}{(R_g + L_g s)^2 + {X_g}^2} \\ \qquad - \frac{{E_{o0}}^2 X_g - E_{o0} V_{g0} \cos\delta_{og0} X_g - E_{o0} V_{g0} \sin\delta_{og0} R_g}{{R_g}^2 + {X_g}^2} \\ k_{pE}(s) = \frac{V_{g0}\sin\delta_{og0} X_g + R_g E_{o0} - R_g V_{g0}\cos\delta_{og0}}{{R_g}^2 + {X_g}^2} \\ \qquad + \frac{E_{o0}(R_g + L_g s)}{(R_g + L_g s)^2 + {X_g}^2} \\ k_{q\delta}(s) = \frac{E_{o0} V_{p0} \sin\delta_{og0} X_g + {E_{o0}}^2 R_g - E_{o0} V_{g0}\cos\delta_{og0} R_g}{{R_g}^2 + {X_g}^2} \\ \qquad - \frac{{E_{o0}}^2 (R_g + L_g s)}{(R_g + L_g s)^2 + {X_g}^2} \\ k_{qE}(s) = \frac{E_{o0} X_g - V_{g0}\cos\delta_{og0} X_g - R_g V_{g0}\sin\delta_{og0}}{{R_g}^2 + {X_g}^2} \\ \qquad + \frac{E_{o0} X_g}{(R_g + L_g s)^2 + {X_g}^2}. \end{cases} \tag{11}$$

It is observed that $k_{p\delta}$(s), k_{pE}(s), $k_{q\delta}$(s), and k_{qE}(s) have the same conjugate poles

$$s_{1,2} = -\frac{R_g}{L_g} \pm j\omega_0 \tag{12}$$

where the ω_0 represents the rated frequency. Under highly inductive impedance, the resistance is small. The poles $s_{1,2}$ are near the virtual axis, and there is a resonance point at ω_0 [24]. It is studied that a pair of conjugate open-loop poles will be brought in, which possibly cause potential instability [7], [8], [9].

Combining (7) and (10), the closed-loop small-signal block diagram of the system can be expressed as Fig. 5. Rewriting the proposed method (7) and the power flow (10) in matrix form as

$$\begin{cases} \tilde{\mathbf{x}} = \mathbf{G}_{t1}(s)\,\tilde{\mathbf{S}}^* - \mathbf{G}_{t2}(s)\,\tilde{\mathbf{S}} \\ \tilde{\mathbf{S}} = \mathbf{G}_f(s)\,\tilde{\mathbf{x}} \end{cases} \tag{13}$$

where $\tilde{\mathbf{x}} = [\tilde{\delta}_o \quad \tilde{E}_0]^T$, $\tilde{\mathbf{S}}^* = [\tilde{P}^* \quad \tilde{Q}^*]^T$, $\tilde{\mathbf{S}} = [\tilde{P} \quad \tilde{Q}]^T$, $\mathbf{G}_{t1}$(s) = diag{m/s, n_d}, $\mathbf{G}_{t2}$(s) = $\begin{bmatrix} \frac{m}{s} + m_d & -m_x \\ n_x & n_d \end{bmatrix}$, and $\mathbf{G}_f$(s) = $\begin{bmatrix} k_{p\delta}(s) & k_{pE}(s) \\ k_{q\delta}(s) & k_{qE}(s) \end{bmatrix}$.

Furthermore, by combining (12) and (13), the closed-loop system equation is obtained as

$$\tilde{\mathbf{S}} = \mathbf{W}(s)\,\tilde{\mathbf{S}}^{*} \tag{14}$$

where $\mathbf{W}(s) = [\mathbf{I} + \mathbf{G}_f(s)\mathbf{G}_{t2}(s)]^{-1}\mathbf{G}_f(s)\mathbf{G}_{t1}(s)$, and $\mathbf{I}$ represents a 2×2 unit matrix. $\mathbf{G}_f(s)$ is stable, and the parameter design easily ensures that $\mathbf{G}_{t1}(s)$ and $\mathbf{G}_{t2}(s)$ are stable. Furthermore, adj$[\mathbf{I} + \mathbf{G}_f(s)\mathbf{G}_{t2}(s)]$ is stable, where "adj" means adjoint matrix. Thus, the system stability depends of the determinant det$[\mathbf{I} + \mathbf{G}_f(s)\mathbf{G}_{t2}(s)]$. If it does not have the right-plane zeros or its Nyquist diagram does not surround the origin, the system is stable.

B. Generalized Power Coupling Characterization Index

Relative Gain Array (RGA) analysis is used to acquire a thorough grasp of coupling properties [25]. In a multivariable system, defining c_i as a controlled variable and m_j as an operational variable. The relative gain Λ_{ij} of channels m_j to c_i can be represented as

$$\Lambda_{ij} = \frac{w_{ij}}{r_{ij}} = \left.\frac{\partial c_i}{\partial m_j}\right|_{\substack{m_k = const \\ (k \neq j)}} \Bigg/ \left.\frac{\partial c_i}{\partial m_j}\right|_{\substack{c_k = const \\ (k \neq i)}} \tag{15}$$

where w_{ij} is the static channel amplification coefficient of the m_j-c_i channel when all other channels are disconnected, which is called the first amplification coefficient. r_{ij} is the static channel amplification coefficient of m_j-c_i channel when all other channels are closed, which is called the second amplification coefficient.

Ordering w_{ij} in subscript order forms the first amplification coefficient matrix $\mathbf{W}(s)$, which is derived from (8)–(14) and $\mathbf{W}(s) = [\mathbf{I} + \mathbf{G}_f(s)\mathbf{G}_{t2}(s)]^{-1}\mathbf{G}_f(s)\mathbf{G}_{t1}(s)$. The diagonal elements $w_{11}(s)$ and $w_{22}(s)$ stand for the closed-loop dynamic response of active and reactive power when the active and reactive power reference fluctuate. Besides, the degree of cross-coupling between reactive and active power is expressed by $w_{12}(s)$ and $w_{21}(s)$. The matrix $\mathbf{W}(s)$ is a frequency-domain matrix, which can quantitatively evaluate the power coupling levels of different frequency bands.

With the first amplification coefficient matrix $\mathbf{W}(s)$, the RGA matrix can be obtained as

$$\mathbf{\Lambda} = \mathbf{W} \otimes \left(\mathbf{W}^{-1}\right)^{T} \tag{16}$$

where $\otimes$ means the multiplication of the same position elements of two matrices. It is worth noting that Λ is independent of the unit of power, and thus, it gives a unified dimensionless generalized PCI.

The rule of power coupling analysis using RGA can be summarized as follows [26].

1) When $\Lambda_{11} > 1$, the two channels are coupled. As Λ_{11} continues to grow, the P and Q cannot be controlled independently.
2) When $0 \leq \Lambda_{11} \leq 1$, the closer Λ_{11} is to 1, the weaker the interaction between the two channels is, and the lower the PCI is. On the contrary, the closer Λ_{11} is to 0, the stronger the interaction between two channels is, and the higher the PCI is.

Therefore, when designing controller parameters, Λ_{11} should be as close to 1 as possible. The effect of the key control parameters m, m_d, m_x, n_d, and n_x on power coupling under three-type line impedance are studied. Λ_{11} with different (a) m, (b) n_d, (c) m_d, (d) n_x, and (e) m_x under $L_g = 4$ mH and $R_g = 0.08\ \Omega$, under $L_g = 2$ mH and $R_g = 0.5\ \Omega$, and under $L_g = 0.01$ mH and $R_g = 2\ \Omega$ are shown in Figs. 6–8, respectively.

When the line impedance is highly inductive, ignoring inductance dynamics, active and reactive power are nearly decoupled which has been discussed in detail in [4] and [5]. Here, the influence of the line inductance dynamics and the control parameters on power coupling is discussed. When discussing the impact of parameters m_d, n_x, and m_x on decoupling performance, the values of droop coefficients are $m = 2\text{e-}4$ and $n_d = 3\text{e-}4$. In Fig. 6(a) and (b), it is observed that decreasing m and n_d can weaken the power coupling in the medium frequency band (MFB), where medium frequency indicates tens to hundreds of Hz. When n_d decreases to a certain degree, Λ_{11} is almost unchanged and is much larger than 1 in the MFB. As shown in Fig. 6(c), it is almost useless to change m_d to promote Λ_{11} closer to 1 in the MFB. When m_d keeps increasing, Λ_{11} keeps away from 1. As Fig. 6(d) and (e) shows, increasing n_x and m_x can effectively suppress the peak value of the MFB, so as to keep Λ_{11} near 1. Therefore, when the line impedance is highly inductive, it is found that different from the traditional P-ω control, the appropriate design of coupling power feedback coefficient (n_x and m_x) is more conducive to decreasing the degree of power coupling in MFB.

When the line impedance is complex resistive-inductive in Fig. 7(a), it is observed that increasing m can reduce the power coupling degree in the low frequency band (LFB), where low frequency indicates a few tenths to several Hz. In Fig. 7(b), when n_d is too large, the Λ_{11} is close to 1 in the LFB but Λ_{11} has a peak value exceeding 1 in the MFB. As n_d continues to decrease, the peak value is suppressed and the power coupling degree increases slightly. In Fig. 7(c), appropriately increasing m_d is conducive to decreasing the degree of power coupling, but when m_d is too large, it will increase the peak value of Λ_{11} in the MFB. In Fig. 7(d) and (e), increasing n_x and m_x make Λ_{11} slightly away from 1 in the LFB. Even though increasing them can effectively suppress the peak value of the MFB.

When the line impedance is highly resistive, as shown in Fig. 8, it is observed that power coupling is serious in the LFB and MFB when m, n_d, and m_d are small. Increasing m, n_d, and m_d can effectively pushes Λ_{11} closer to 1, and the effect of increasing n_d to help decreasing the degree of power coupling is the best.

In conclusion, the main frequency bands of decreasing the degree of power coupling are different under three types of line impedances. When the line impedance is highly inductive, the main contradiction concerned about is the power coupling in the MFB, and increasing m_x and n_x help decrease the power coupling in the MFB. However, when the line impedance is highly resistive, the main contradiction is the power coupling in the LFB and the MFB, and increasing m and n_d will reduce the power coupling of the two frequency bands.

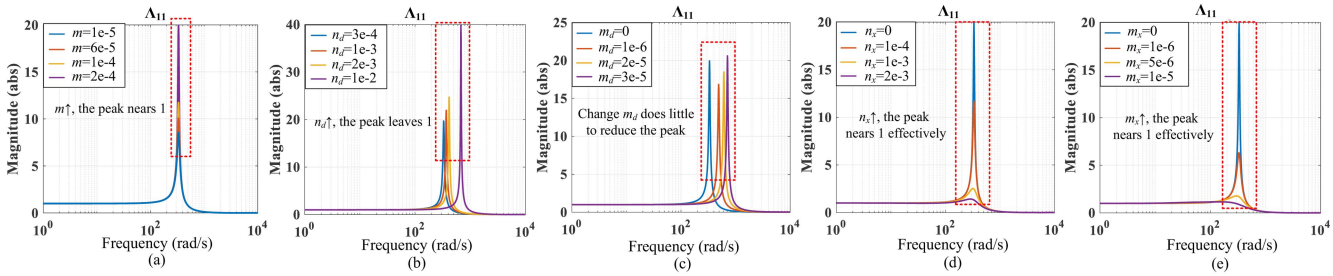

Fig. 6. Λ_{11} with different (a) m, (b) n_d, (c) m_d, (d) n_x, and (e) m_x under $L_g = 4$ mH and $R_g = 0.08\ \Omega$.

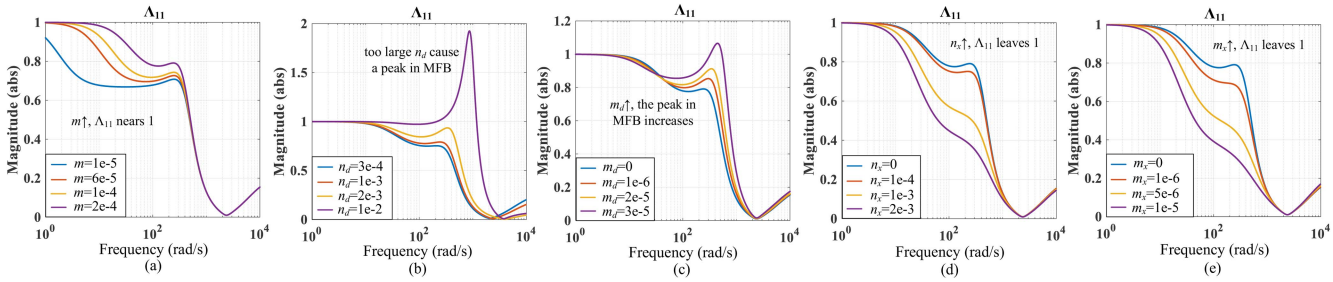

Fig. 7. Λ_{11} with different (a) m, (b) n_d, (c) m_d, (d) n_x, and (e) m_x under $L_g = 2$ mH and $R_g = 0.5\ \Omega$.

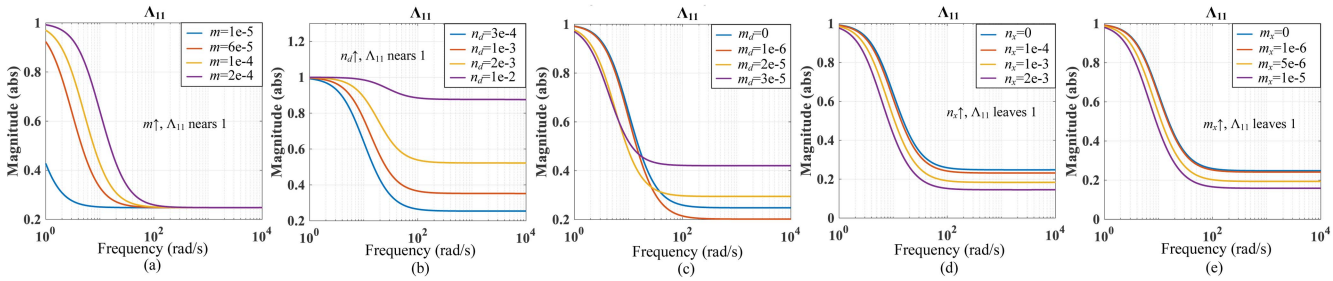

Fig. 8. Λ_{11} with different (a) m, (b) n_d, (c) m_d, (d) n_x, and (e) m_x under $L_g = 0.01$ mH and $R_g = 2\ \Omega$.

C. Small-Signal Stability Analysis

To confirm the broad applicability of the unified inverter control framework under various line impedance, root trajectories are carried out for systems with highly-inductive, equally resistive-inductive, and highly-resistive line impedances. The effect of the control parameters m, m_d, m_x, n_d, and n_x on system stability are studied. The root locus of $\det(\mathbf{I} + \mathbf{G}_f(s)\mathbf{G}_t(s))$ with a) $m \in$ [1e-5, 1e-3], b) $n_d \in$ [1e-4, 1e-2], c) $m_d \in$ [0, 1e-4], d) $n_x \in$ [0, 2e-3], e) $m_x \in$ [0, 1e-5] under $L_g = 4$ mH and $R_g = 0.08\ \Omega$, under $L_g = 2$ mH and $R_g = 0.5\ \Omega$, and under $L_g = 0.01$ mH and $R_g = 2\ \Omega$ are shown in Figs. 9–11. The following features can be drawn.

1) Considering the inductance dynamics, there are a pair of medium-frequency (MF) roots $\lambda_{1,2}$ and a root λ_3 mainly affecting the system stability and dynamic response. Under the highly inductive line impedance, the MF roots $\lambda_{1,2}$, which are easily unstable. With the decrease of line inductance and the increase of the line resistance, the MF roots $\lambda_{1,2}$ are further away from the imaginary axis and are more stable. Under the highly resistive line impedance, the root λ_3 is close to the imaginary axis that may increase the system adjusting time.
2) Under the highly inductive and equally resistive-inductive line impedance, decreasing m and increasing m_d help stabilize the MF roots $\lambda_{1,2}$ but also makes the root λ_3 substantially close to the origin, which slows down the system response speed. Thus, it is not the best choice to improve the stability of the roots $\lambda_{1,2}$. With the proposed method, increasing coupling feedback coefficient m_x and n_x, the MF roots $\lambda_{1,2}$ are significantly far away from the imaginary axis, which increases the system damping and inhibits the MF oscillation and is conducive to the stability of the roots $\lambda_{1,2}$. Moreover, the sensitivity of root λ_3 to

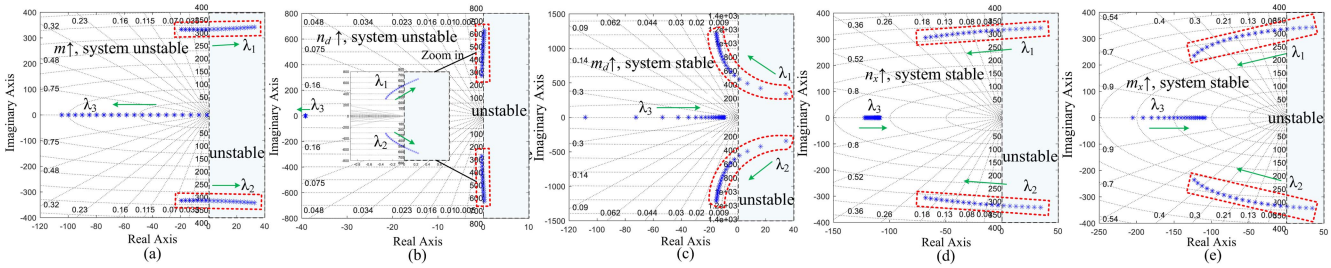

Fig. 9. Case1 (under highly inductive impedance): Root locus with (a) $m \in$ [1e-5, 1e-3], (b) $n_d \in$ [1e-4, 1e-2], (c) $m_d \in$ [0, 1e-4], (d) $n_x \in$ [0, 2e-3], (e) $m_x \in$ [0, 1e-5].

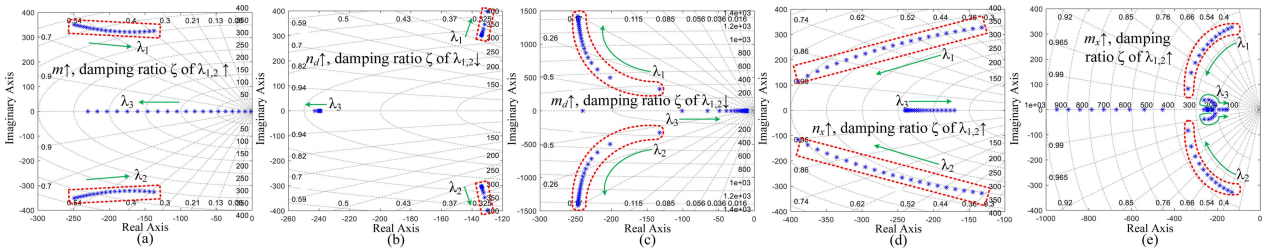

Fig. 10. Case2 (under complex resistive-inductive impedance): Root locus with (a) $m \in$ [1e-5, 1e-3], (b) $n_d \in$ [1e-4, 1e-3], (c) $m_d \in$ [0, 1e-4], (d) $n_x \in$ [0, 2e-3], (e) $m_x \in$ [0, 1e-5].

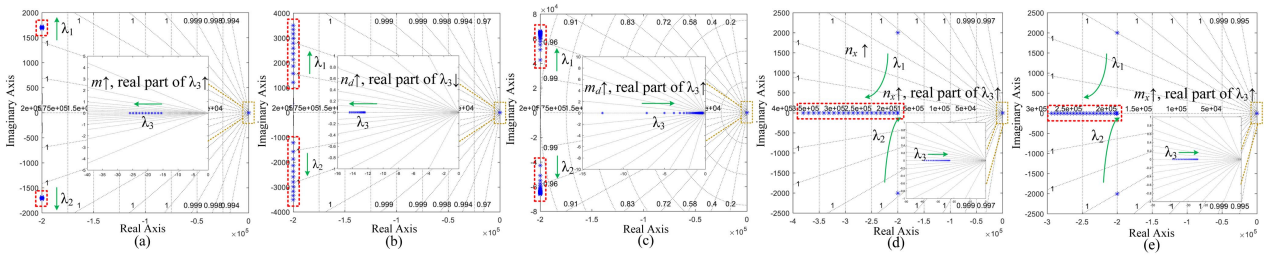

Fig. 11. Case3 (under highly resistive impedance): Root locus with (a) $m \in$ [1e-5, 1e-3], (b) $n_d \in$ [1e-4, 1e-3], (c) $m_d \in$ [0, 1e-4], (d) $n_x \in$ [0, 2e-3], (e) $m_x \in$ [0, 1e-5].

parameters m_x and n_x is obviously lower than that of the parameters m and m_d.

3) Under three-types line impedance, increasing n_d moves $\lambda_{1,2}$ away from the real axis, i.e., small n_d is beneficial to damping the MF roots $\lambda_{1,2}$. When the line impedance is highly resistive, the adverse effect on MF roots $\lambda_{1,2}$ is negligible since it is far away from the imaginary axis and decays rapidly. In this case, m and n_d should be large, since large m and n_d move λ_3 away from the imaginary axis that speeds up the system dynamic response. Besides, in this case even if n_d is set to 0, the system can still be stable by the weak coupling between P and ω ($\tilde{P} \approx E_{o0}V_{g0}\sin\delta_{og0}R_g\tilde{\delta}_o/{Z_g}^2$) where $\sin\delta_{og0}$ is small). However, the dynamic response is slow and the adjusting time is too long.

Fig. 12 summarizes the parameters control design according to the different degrees of power coupling in different frequency bands and system stability, where $(\Lambda_{11}-1)$ represents the degree of Λ_{11} deviating from 1. The closer $(\Lambda_{11}-1)$ is to 0, the weaker the power coupling. It can be summarized as follows.

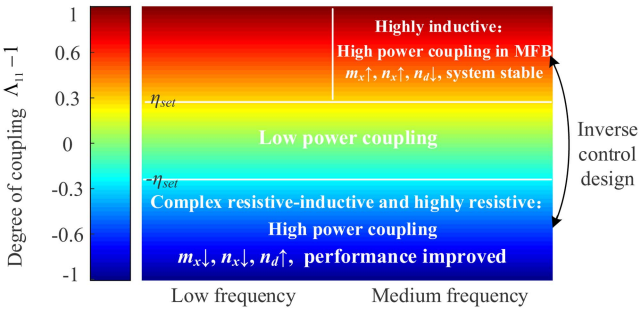

Fig. 12. Control parameter design guideline under different degree of power coupling ($(\Lambda_{11}-1)$ closer to 0 indicates a weaker power coupling).

1) $-\eta_{\text{set}} < (\Lambda_{11}-1) < \eta_{\text{set}}$ represents the low degree of power coupling, which the parameters should be designed to satisfy, where η_{set} is the desired degree of power coupling.
2) $(\Lambda_{11}-1) > \eta_{\text{set}}$ and $(\Lambda_{11}-1) < \eta_{\text{set}}$ represent high power coupling. However, these two cases have inverse

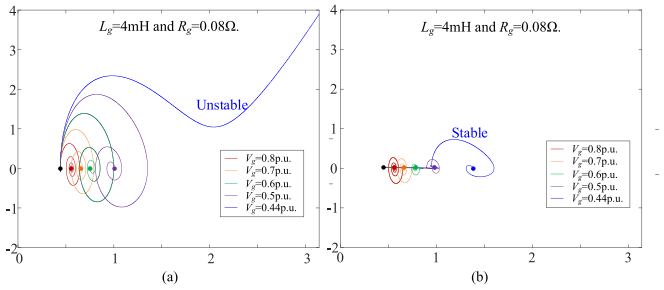

Fig. 13. Phase portraits under different grid voltage sags with $L_g = 4$ mH and $R_g = 0.08$ Ω: (a) Traditional GFM method (b) proposed method with $m_x =$ 4e-6, $m_d = 0$, $n_x =$ 4e-4.

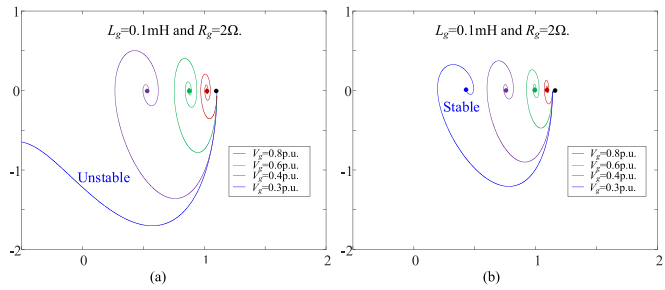

Fig. 15. Phase portraits under different grid voltage sags with $L_g = 0.1$ mH and $R_g = 2$ Ω: (a) Traditional GFM method (b) proposed method with $m_x =$ 1e-6, $m_d =$ 5e-6, $n_x =$ 1e-4.

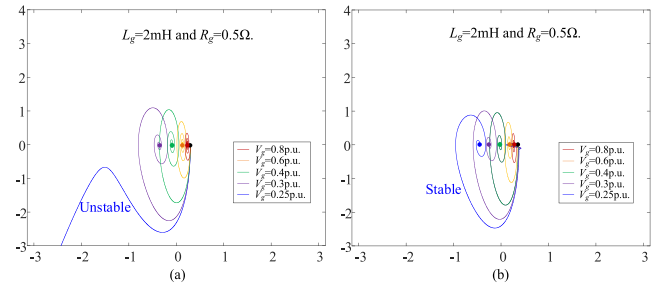

Fig. 14. Phase portraits under different grid voltage sags with $L_g = 2$ mH and $R_g = 0.5$ Ω: (a) Traditional GFM method (b) proposed method with $m_x =$ 2e-6, $m_d =$ 5e-6, $n_x =$ 2e-4.

control design. When $(\Lambda_{11} - 1) > \eta_{\text{set}}$ in the MFB, increasing n_x and m_x, and decreasing n_d help decrease the degree of power coupling in the MFB and are conducive to system stability. When $(\Lambda_{11} - 1) < \eta_{\text{set}}$, decreasing n_x and m_x, and increasing n_d help decrease the degree of power coupling and help speed up the adjusting time.

D. Large-Signal Stability Analysis

This part conducts a comparative analysis of large-signal stability between the proposed method and traditional grid-forming (GFM) methods, i.e., VSG control [27], [28] under complex line impedance. The parameters of the proposed method are designed according to the design rules under different line X/R ratio that are concluded in the above part. Phase portrait analysis [29], [30] is implemented. The phase portraits of traditional grid-forming control methods and the proposed method with highly inductive, complex resistive-inductive, and highly resistive line impedance are listed in Figs. 13–15, respectively. It is observed that the proposed method, which follows the parameter design rule also help enhance large-signal stability under grid voltage sags.

E. Parameters Design Guidelines

Improper parameter design may lead to poor dynamic performance of the system. Combining the above analysis, the design rules of the parameters can be summarized as follows.

1) *Under highly inductive line impedance*, the medium frequency oscillation is serious, and may even lead to system instability. Meanwhile, the power coupling degree is strong in the medium frequency band and PCI Λ_{11} is much greater than 1. Therefore, n_x and m_x should be large, which can effectively reduce the power coupling degree in the MFB, and suppress the medium frequency oscillation. When an additional voltage drop is not desired, setting $n_x = 0$. Besides, the effect on the pole λ_3 is small that does not slow down the response.
2) *Under highly resistive line impedance*, the poles $\lambda_{1,2}$ are far away from the imaginary axis, and its damping ratio is large. However, the root λ_3 is close to the imaginary axis that may increase the adjusting time, and the power coupling degree in the LFB is very strong. Therefore, n_x and m_x can be set to 0. m_d and n_d should be large, which help reduce the degree of power coupling, and its value can be referred to (5).
3) *Under complex resistive-inductive line impedance*, the damping ratio of conjugate poles $\lambda_{1,2}$ and power coupling in the low-frequency band should be considered synthetically. n_x and m_x should be small, and m_d and n_d should be increased appropriately to reduce the degree of power coupling and speed up the adjusting time.

To comprehensively consider the overall systematic dynamic performance, such as suppressing medium frequency oscillation, decreasing the degree of power coupling and reducing adjusting time, the optimization problem of control design can be constructed from the PCI-oriented perspective

$$\min\ J = \left(\max\left|1 - \Lambda_{11}\left(j2\pi f\right)\right|_{f \le f_{mo}}\right)^2 \tag{17}$$

Subject to:

$$0 < m \le \frac{\omega_{\max} - \omega_{\min}}{P_{\max} - P_{\min}} \tag{18a}$$

$$0 < n_d\left(Q_{\max} - Q_{\min}\right) + n_x P_{\max} \le V_{\max} - V_{\min} \tag{18b}$$

$$\sigma \le \sigma^* \tag{18c}$$

$$\zeta \ge \zeta^* \tag{18d}$$

$$\max\left|1 - \Lambda_{11}\left(j2\pi f\right)\right|_{f \le f_{mo}} \le \eta_{\text{set}} \tag{18e}$$

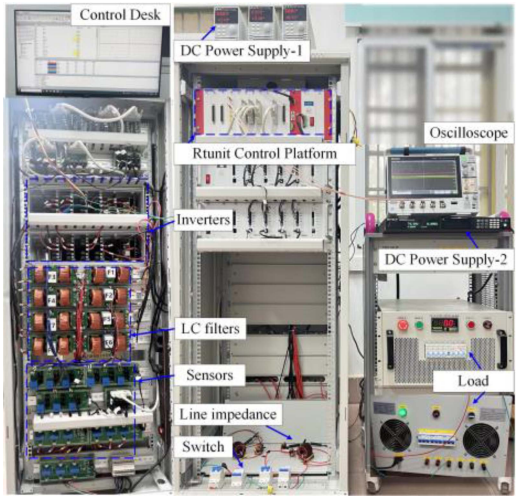

Fig. 16. Experimental setups of the two parallel system.

TABLE II
CHIL PARAMETERS

Control Parameter	
AC voltage reference V^*/ω^*	156V/314rad/s
Dc-side voltage	180 V
PWM frequency f_{PWM}	10 kHz
Sampling time T_s	1e-4s
Filter inductance/capacitor L_f/C_f	1.8 mH/25 μF
Low-pass filter cut-off frequency ω_c	30×2π rad/s
Case1: highly inductive line impedance	L_1 = 1.5 mH, L_2 =2.2 mH
Case2: complex R-L line impedance	L_1 = 0.7 mH, R_1 = 0.4 Ω L_2 = 0.96 mH, R_2 = 0.2 Ω
Case3: highly resistive line impedance	R_1 = 0.5 Ω, R_2 = 0.7 Ω

where $\omega_{\min}$ and $\omega_{\max}$ represents the lower and upper bounds of the allowable range of system angular frequency. ζ and σ are the damping ratio and the real part of the eigenvalues that are calculated by (14). ζ^* and σ^* are the set minimum damping ratio and real part that determines the damping margin and system response speed. f_{mo} is the medium frequency of the oscillation. Constraints of the steady-state frequency sag (18a), voltage quality (18b), system stability margin (18c) and (18d) are comprehensively considered. Besides, the maximum degree of power coupling is limited below η_{set} as (18e) shows, which can be calculated by (16).

IV. CASE STUDY

A. Hardware Experiment Results

The hardware experiment results are displayed to test the adaptability and effectiveness of the unified inverter control framework under various line impedances (highly inductive, complex impedance, and highly resistive), and the experimental setup is shown in Fig. 16. It includes two inverters, two dc power supplies, a rtunit controller, and resistance loads. The rtunit platform accomplishes programming tasks based on MATLAB/Simulink. The experimental parameters are listed in Table II.

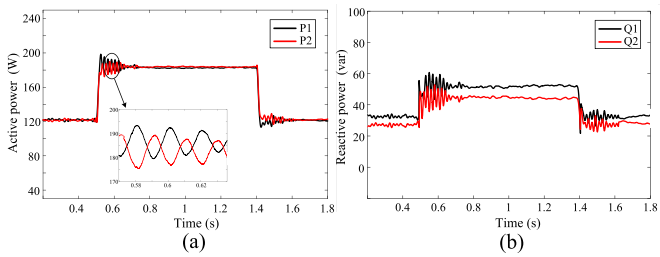

Fig. 17. Waveforms under conventional droop control, i.e., $m_d = 0$, $m_x = 0$, $n_x = 0$. (a) Active power. (b) Reactive power.

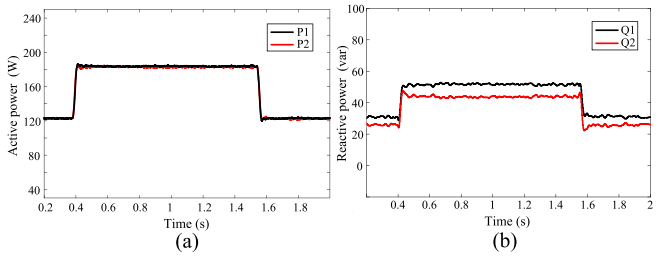

Fig. 18. Waveforms under proposed method. (a) Active power. (b) Reactive power.

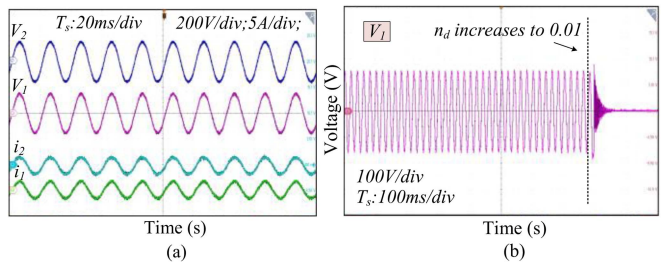

Fig. 19. (a) Output voltage and current of two inverters. (b) Output voltage of VSC1 with droop control when n_d increases to 0.01.

1) Under Highly Inductive Line Impedance: Figs. 17 and 18 show the power of two inverters under load disturbance with conventional droop control, i.e., $m_d = 0$, $m_x = 0$, $n_x = 0$, and the unified control framework, when the line impedance is highly inductive. The control parameters of VSCs under the unified control frame in this case are set as m_1 = 1e-3, n_{d1} = 8e-4, m_{d1} = 0, m_{x1} = 4e-4, n_{x1} = 1.1e-3, and m_2 = 1e-3, n_{d2} = 5e-4, m_{d2} = 0, m_{x2} = 4e-4, n_{x2} = 2e-3, according to the optimal parameters design guidelines (17). As Fig. 17 shows, at 0.5 s, a load disturbance is introduced. It can be seen that with the conventional P-ω droop control, the system occurs serious medium frequency oscillation. After measurement, the oscillation frequency of the system is 47.2 Hz. It is observed from Fig. 18 that the medium frequency oscillation is suppressed effectively with proper design of m_x and n_x, which proves the correctness of root locus analysis. Compared to the virtual resistance method, there is more freedom of the proposed method. Besides, frequency self-synchronizing is realized and precise active power sharing between two inverters is guaranteed. The output voltage and current of two inverters are shown in Fig. 19(a). Fig. 19(b) shows

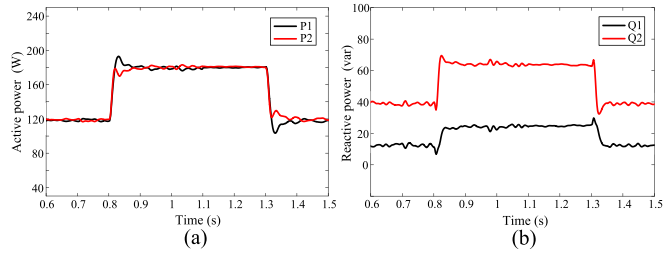

Fig. 20. Waveforms under conventional droop control, i.e., $m_d = 0$, $m_x = 0$, $n_x = 0$. (a) Active power. (b) Reactive power.

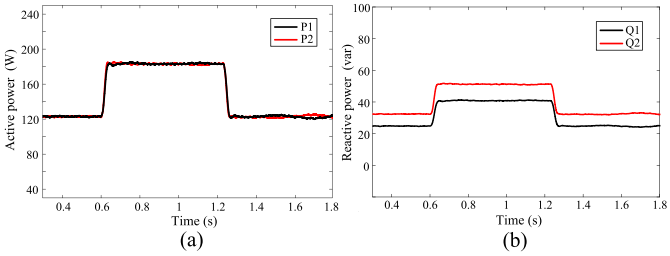

Fig. 21. Waveforms under proposed method. (a) Active power. (b) Reactive power.

the output voltage of VSC1 with conventional droop control when n_d increases to 0.01. It is seen that a large n_d makes the system eventually lose its stability when the line impedance is highly inductive.

2) Under Complex Resistive-Inductive Line Impedance: Figs. 20 and 21 show the power of two inverters under load disturbance with conventional droop control, i.e., $m_d = 0$, $m_x = 0$, $n_x = 0$, and the unified control framework, when the line impedance is complex resistive-inductive. The parameters of VSCs in this case are set as $m_1 =$ 1e-3, $m_{d1} =$ 1.5e-5, $n_{d1} =$ 0.0151, $m_{x1} = 0$, $n_{x1} =$ 1e-4, and $m_2 =$ 1e-3, $n_{d2} = 0.02$, $m_{d2} = 0$, $m_{x2} =$ 1e-5, $n_{x2} =$ 6e-4. At 0.6 s, a load disturbance is introduced. It is observed that active power sharing is ensured before and after load disturbance and the power dynamic response is fine during the load disturbance with the proposed control framework. The experimental waveform results are not much different from what happens when the line impedance is highly inductive. To ensure better decoupling of reactive and active power in the case of complex impedance, the value of m_d is appropriately increased. Besides, the dynamic and steady-state performance of the system is little affected by the increase of the line resistance.

3) Under Highly Resistive Line Impedance: The output active power with the conventional droop control, i.e., $m_d = 0$, $m_x = 0$, $n_x = 0$, and the unified control framework under load disturbance is shown in Figs. 22 and 23, respectively. The parameters of VSCs in this case are set as $m_1 =$ 1e-3, $m_{d1} =$ 5e-5, $n_{d1} = 0.0283$, $m_{x1} = 0$, $n_{x1} = 0$, and $m_2 =$ 1e-3, $n_{d2} =$ 0.0351, $m_{d2} =$ 6e-5, $m_{x2} = 0$, $n_{x2} = 0$. As Fig. 19 shows, at 1 s, a load disturbance is introduced. The P and δ (or Q and V) are coupled weakly when the line impedance is highly resistive. Thus, it results in too long adjusting time and poor control

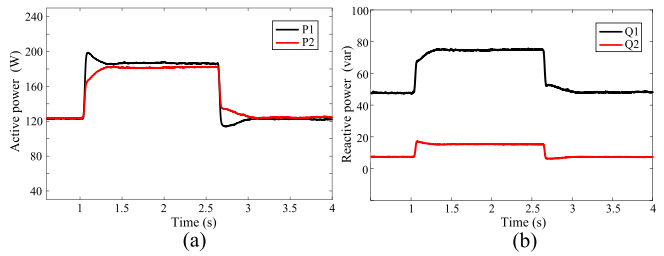

Fig. 22. Waveforms under conventional droop control, i.e., $m_d = 0$, $m_x = 0$, $n_x = 0$. (a) Active power. (b) Reactive power.

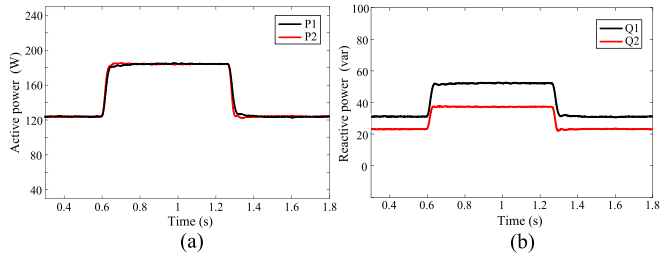

Fig. 23. Waveforms under proposed method. (a) Active power. (b) Reactive power.

TABLE III
PARAMETERS DESIGN GUIDELINE

Line characteristic	Parameter design guideline
Case1: highly inductive	➢ Large n_d harms system stability. ➢ Increasing m_x/n_x suppress MF power oscillation.
Case2: complex resistive-inductive	➢ Increasing m_d and n_d reduces power coupling degree.
Case3: highly resistive	➢ Small n_d results in too long adjusting time. ➢ Increasing m_d/n_d reduces power coupling degree and speeds up adjusting time.

performance under conventional P-ω control with inappropriate parameters. To strengthen the connection between P and ω, n_d and m_d is appropriately increased. From Fig. 23, it is observed that the active power of the two inverters before and after load disturbance has been evenly divided with fine dynamic response speed. Besides, the consequences of frequency synchronization are essentially identical to those consequences obtained under highly inductive and equally resistive-inductive line impedance.

Based on the experimental results of the above three cases, it is concluded that [P Q]-[ω V] interactive control framework ensures universal applicability under highly inductive, complex resistive-inductive, and highly resistive line impedances. It also ensures frequency synchronization and accurate active power sharing. Besides, the parameter control design under the three-line impedances are summarized in Table III.

4) Applicability When the Ratio of X/R Changes: To verify the practicality of the proposed unified control framework, the waveforms of output active and reactive power with the unified control framework when the X/R of the line impedance changes is shown in Fig. 24. The parameters of VSCs in this case are set as $m_1 =$ 1e-3, $m_{d1} =$ 0.11e-5, $n_{d1} = 0.0125$, $m_{x1} =$ 0.21e-5, $n_{x1} =$ 0.61e-3, and $m_2 =$ 1e-3, $n_{d2} = 0.0126$, $m_{d2} =$ 0.15e-5, $m_{x2} =$ 0.22e-5, $n_{x2} =$ 0.64e-3. As Fig. 21 shows, around 0.6 s,

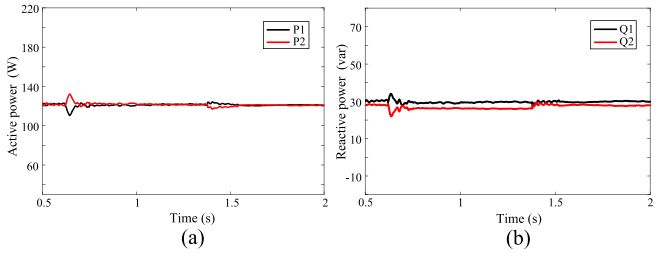

Fig. 24. Waveforms under proposed method when the X/R changes. (a) Active power. (b) Reactive power.

Fig. 25. Configuration of the CHIL system.

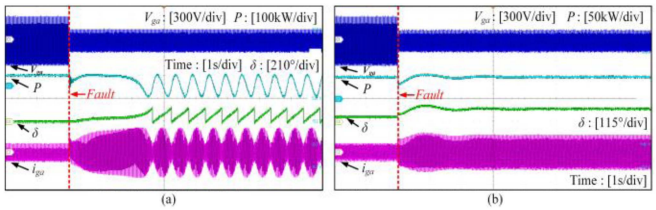

Fig. 26. Waveforms of grid voltage, active power, phase angle, and current when grid voltage drops to 0.44 p.u. with highly inductive impedance: $L_g = 4$ mH and $R_g = 0.08\ \Omega$.

the line resistance is $R_1 = R_2 = 0.2\ \Omega$, and line inductance changes from $L_1 = 0.7$ mH, $L_2 = 0.96$ mH to $L_1 = 4$ mH, $L_2 = 4.5$ mH, i.e., the ratio of X/R changes from about 6 to 1. Around 1.4 s, the ratio of X/R changes from about 1 to 6. It is observed that the proposed method still works and the system possesses good dynamic performance when the X/R of the line impedance changes within a certain range. The selection range of control parameters is relatively wide and has certain robustness.

B. Control Hardware-in-Loop Experiment Results

To verify the large-signal stability analysis, the control-hardware-in-loop (CHIL) experimental results are displayed. The experimental setup is shown in Fig. 25. The main circuit is emulated in the OPAL-RT4510 simulator, which contains three-phase converter, filters, and grid. The controller of the inverter is implemented in the digital signal processing (DSP) control board.

Fig. 26 shows the comparative waveforms of grid voltage, active power, phase angle, and current when grid voltage drops to 0.44 p.u. with highly inductive impedance: $L_g = 4$ mH and $R_g = 0.08\ \Omega$: a) traditional GFM method and b) the proposed method. Fig. 27 shows the comparative waveforms when grid voltage drops to 0.25 p.u. with complex resistive-inductive impedance: $L_g = 2$ mH and $R_g = 0.5\ \Omega$. Fig. 28 shows the comparative waveforms when grid voltage drops to 0.3 p.u. with highly resistive impedance: $L_g = 0.1$ mH and $R_g = 2\ \Omega$. Based on the results, it is observed that the proposed method, which follows the parameter design rule, as concluded in Sections I and III help enhance large-signal stability under grid voltage sags. Besides, it is consistent with the results of phase portrait analysis.

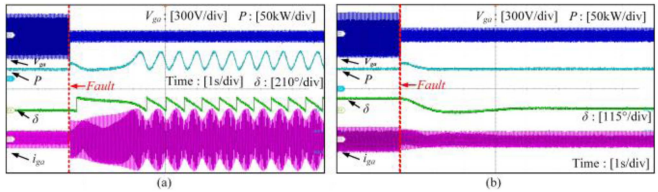

Fig. 27. Waveforms of grid voltage, active power, phase angle, and current when grid voltage drops to 0.25 p.u. with complex resistive-inductive impedance: $L_g = 2$ mH and $R_g = 0.5\ \Omega$.

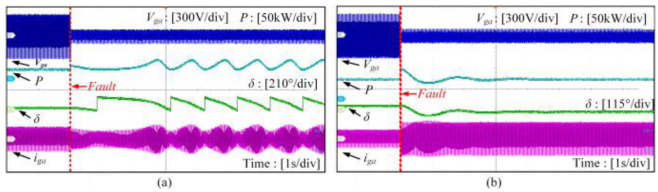

Fig. 28. Waveforms of grid voltage, active power, phase angle, and current when grid voltage drops to 0.3 p.u. with highly resistive impedance: $L_g = 0.1$ mH and $R_g = 2\ \Omega$.

V. Conclusion

To clarify the quantitative power coupling relationship and corresponding control design under different line impedances, PCI-oriented stability analysis and interaction control design for inverter-based microgrid under complex R/X ratio are conducted. To this issue, a generalized PCI is designed based on RGA under a unified [P Q]-[ω V] interactive control framework. In particular, new perspectives of control parameter design under different line impedances are given that the design rules of droop control parameters between highly-inductive and highly-resistive line impedances are totally inverse. Comparative experiments verify the effectiveness of the proposed method and control design. The proposed method suppresses medium-frequency power oscillation under highly inductive line impedance, decreases the degree of power decoupling and speeds up adjusting time under highly resistive and complex resistive-inductive line impedance. Furthermore, professional design for realistic distribution network, and the influence mechanism analysis of power coupling on the transient stability and the attractive region estimation under large disturbance fault are also the focus of our future research.

REFERENCES

[1] M. Z. Mansour, S. P. Me, S. Hadavi, B. Badrazadeh, A. Karimi, and B. Bahrani, "Nonlinear transient stability analysis of phase-locked loop based grid-following voltage source converters using Lyapunov's direct method," *IEEE Trans. Emerg. Sel. Topics Power Electron.*, vol. 10, no. 3, pp. 2699–2709, Jun. 2022.

[2] Y. S. Chen, X. Hou, H. Han, S. Fu, and M. Su, "Quantitative parameters design of VSG oriented to transient synchronization stability," *IEEE Trans. Power Syst.*, vol. 38, no. 5, pp. 4978–4981, Sep. 2023.

[3] F. Milano, F. Dörfler, G. Hug, D. J. Hill, and G. Verbic, "Foundations and challenges of low-inertia systems," in *Proc. Power Syst. Comput. Conf.*, 2018, pp. 1–25.

[4] M. C. Chandorkar, D. M. Divan, and R. Adapa, "Control of parallel connected inverters in standalone AC supply systems," *IEEE Trans. Ind. Appl.*, vol. 29, no. 1, pp. 136–143, Jan./Feb. 1993.

[5] N. Pogaku, M. Prodanovic, and T. C. Green, "Modeling, analysis and testing of autonomous operation of an inverter-based microgrid," *IEEE Trans. Power Electron.*, vol. 22, no. 2, pp. 613–625, Mar. 2007.

[6] J. M. Guerrero, L. Garcia de Vicuna, J. Matas, M. Castilla, and J. Miret, "Output impedance design of parallel-connected UPS inverters with wireless load-sharing control," *IEEE Trans. Ind. Electron.*, vol. 52, no. 4, pp. 1126–1135, Aug. 2005.

[7] L. Zhang, L. Harnefors, and H.-P. Nee, "Power-synchronization control of grid-connected voltage-source converters," *IEEE Trans. Power Syst.*, vol. 25, no. 2, pp. 809–820, May 2010.

[8] L. Harnefors, M. Hinkkanen, U. Riaz, F. M. M. Rahman, and L. Zhang, "Robust analytic design of power-synchronization control," *IEEE Trans. Ind. Electron.*, vol. 66, no. 8, pp. 5810–5819, Aug. 2019.

[9] S. Chen, Y. Sun, H. Han, S. Fu, S. Luo, and G. Shi, "A modified VSG control scheme with virtual resistance to enhance both small-signal stability and transient synchronization stability," *IEEE Trans. Power Electron.*, vol. 38, no. 5, pp. 6005–6014, May 2023.

[10] X. Wang, M. G. Taul, H. Wu, Y. Liao, F. Blaabjerg, and L. Harnefors, "Grid synchronization stability of converter-based resources—An overview," *IEEE Open J. Ind. Appl.*, vol. 1, pp. 115–134, Aug. 2020.

[11] J. M. Guerrero, J. Matas, L. Garcia de Vicuna, M. Castilla, and J. Miret, "Decentralized control for parallel operation of distributed generation inverters using resistive output impedance," *IEEE Trans. Ind. Electron.*, vol. 54, no. 2, pp. 994–1004, Apr. 2007.

[12] A. Rodriguez-Cabero, J. Roldan-Perez, and M. Prodanovic, "Virtual impedance design considerations for virtual synchronous machines in weak grids," *IEEE Trans. Emerg. Sel. Topics Power Electron.*, vol. 8, no. 2, pp. 1477–1489, Jun. 2020.

[13] T. Wen, X. Zou, D. Zhu, X. Guo, L. Peng, and Y. Kang, "Comprehensive perspective on virtual inductor for improved power decoupling of virtual synchronous generator control," *IET Renewable Power Gener.*, vol. 14, no. 4, pp. 485–494, 2020.

[14] J. He and Y. W. Li, "Analysis, design, and implementation of virtual impedance for power electronics interfaced distributed generation," *IEEE Trans. Ind. Appl.*, vol. 47, no. 6, pp. 2525–2538, Nov./Dec. 2011.

[15] K. De Brabandere, B. Bolsens, J. Van den Keybus, A. Woyte, J. Driesen, and R. Belmans, "A voltage and frequency droop control method for parallel inverters," *IEEE Trans. Power Electron.*, vol. 22, no. 4, pp. 1107–1115, Jul. 2007.

[16] Y. Li and Y. W. Li, "Decoupled power control for an inverter based low voltage microgrid in autonomous operation," in *Proc. IEEE 6th Int. Power Electron. Motion Control Conf.*, 2009, pp. 2490–2496.

[17] Y. Li and Y. W. Li, "Power management of inverter interfaced autonomous microgrid based on virtual frequency-voltage frame," *IEEE Trans. Smart Grid*, vol. 2, no. 1, pp. 30–40, Mar. 2011.

[18] X. Yan and Y. Zhang, "Power coupling analysis of inverters based on relative gain method and decoupling control based on feedforward compensation," in *Proc. Int. Conf. Renewable Power Gener.*, 2015, pp. 1–5.

[19] Y. Zhang and U. Raheja, "An optimized virtual synchronous generator control strategy for power decoupling in grid connected inverters," in *Proc. IEEE Energy Convers. Congr. Expo.*, 2019, pp. 49–54.

[20] M. Chen, D. Zhou, A. Tayyebi, E. Prieto-Araujo, F. Dörfler, and F. Blaabjerg, "Generalized multivariable grid-forming control design for power converters," *IEEE Trans. Smart Grid*, vol. 13, no. 4, pp. 2873–2885, Jul. 2022.

[21] D. B. Rathnayake and B. Bahrani, "Multivariable control design for grid-forming inverters with decoupled active and reactive power loops," *IEEE Trans. Power Electron.*, vol. 38, no. 2, pp. 1635–1649, Feb. 2023.

[22] M. Chen, D. Zhou, and F. Blaabjerg, "Multivariable grid-forming converters with direct states control," *IEEE Trans. Ind. Appl.*, vol. 59, no. 4, pp. 4334–4341, Jul./Aug. 2023.

[23] M. Chen, D. Zhou, A. Tayyebi, E. Prieto-Araujo, F. Dörfler, and F. Blaabjerg, "On power control of grid-forming converters: Modeling, controllability, and full-state feedback design," *IEEE Trans. Sustain. Energy*, vol. 15, no. 1, pp. 68–80, Jan. 2024.

[24] X. Zhang et al., "Analysis of dynamic power angle oscillation and its suppression strategy for the droop-controlled grid-connected inverter," *IEEE J. Emerg. Sel. Topics Power Electron.*, vol. 9, no. 5, pp. 5718–5731, Oct. 2021.

[25] E. Bristol, "On a new measure of interaction for multivariable process control," *IEEE Trans. Autom. Control*, vol. 11, no. 1, pp. 133–134, Jan. 1966.

[26] F. G. Shinskey, *Process Control Systems: Application, Design, and Adjustment*, 3rd ed. New York, NY, USA: McGraw-Hill, 1988 pp. 181–203.

[27] Q. C. Zhong and G. Weiss, "Synchronverters: Inverters that mimic synchronous generators," *IEEE Trans. Ind. Electron.*, vol. 58, no. 4, pp. 1259–1267, Apr. 2011.

[28] H. Bevrani, T. Ise, and Y. Miura, "Virtual synchronous generators: A survey and new perspectives," *Int. J. Elect. Power Energy Syst.*, vol. 54, pp. 244–254, 2014.

[29] H. Wu and X. Wang, "Design-oriented transient stability analysis of grid-connected converters with power synchronization control," *IEEE Trans. Ind. Electron.*, vol. 66, no. 8, pp. 6473–6482, Aug. 2019.

[30] D. Pan, X. Wang, F. Liu, and R. Shi, "Transient stability of voltage-source converters with grid-forming control: A design-oriented study," *IEEE J. Emerg. Sel. Topics Power Electron.*, vol. 8, no. 2, pp. 1019–1033, Jun. 2020.

Siqi Fu received the B.S. degree in electrical engineering and the automatization from the Hefei University of Technology, Anhui, China, in 2018, and the Ph.D. degree in control science and engineering from the School of Automation, Central South University, Changsha, China, in 2024.

She is currently a Lecturer with the College of Electronic Information and Electrical Engineering, Changsha University, Changsha, China. Her research interests include control and stability of distributed microgrid and power-electronic-enabled power network.

Yao Sun (Member, IEEE) received the B.S. degree in automation and the M.S. and Ph.D. degrees in control engineering from Central South University Changsha, China, in 2004, 2007, and 2010, respectively.

He was a Professor with the School of Automation, Central South University, Changsha, China. His research interests include matrix converter, microgrid, and wind energy conversion system.

Xiaochao Hou (Member, IEEE) received the B.S., M.S., and Ph.D. degrees in control science and engineering from the School of Automation, Central South University, Changsha, China, in 2014, 2017, and 2020, respectively.

From 2018 to 2019, he was a was the Ph.D. student with Nanyang Technological University, Singapore. From 2020 to 2022, he was a Postdoctoral Fellow with the Department of Electrical Engineering, Tsinghua University, China. From Apr. 2023, he is currently an Associate Professor with the School of Electronic Information, Central South University, Changsha, China. His research interests include distributed PV/ESS/EV integrations, and series/parallel-type microgrid system.

Feng Zhou received the B.Eng., M.Eng., and Ph.D. degrees in control science and engineering from Central South University, Changsha, China, in 2009, 2012, and 2017, respectively.

He is currently an Associate Professor with the College of Electronic Information and Electrical Engineering, Changsha University, Changsha, China. His research interests include power electronics, adjustable speed drives, and wind energy conversion.

Mei Su received the B.S. degree in automation, and the M.S. and Ph.D. degrees in control engineering from the School of Information Science and Engineering, Central South University, Changsha, China, in 1989, 1992, and 2005, respectively.

She was a Full Professor with the School of Automation, Central South University. Her research interests include matrix converter, adjustable speed drives, and wind energy conversion.

Prof. Su is currently an Associate Editor of IEEE TRANSACTIONS ON POWER ELECTRONICS.

Xin Zhang (Senior Member, lEEE) received the Ph.D. degree in automatic control and systems engineering from the University of Sheffeld, Sheffeld, U.K., in 2016, and the Ph.D. degree in electronic and electrical engineering from Nanjing University of Aeronautics and Astronautics, Nanjing, China, in 2014.

From 2017 to 2020, he was an Assistant Professor of Power Engineering with the School of Electrical and Electronic Engineering, Nanyang Technological University, Singapore. He is currently a Research Professor with College of Electrical Engineering, Zhejiang University, Zhejiang, China. He was a Postdoctoral Research Fellow with City University of Hong Kong, Hong Kong, from Jan. to Sep. 2017 and a Research Associate with The University of Sheffeld from 2014 to 2016. His research interests include power electronics, power system, and advanced control theory, together with their applications in various sectors.

Kai Sun (Fellow, IEEE) received the B.E., M.E., and Ph.D. degrees in electrical engineering from Tsinghua University, Beijing, China, in 2000, 2002, and 2006, respectively.

In 2006, he was with the Faculty of Electrical Engineering. Tsinghua University, where he is currently a Tenured Associate Professor. From 2009 to 2010, he was a Visiting Scholar with the Department of Energy Technology, Aalborg University, Aalborg, Denmark. From Jan. to Aug. 2017, he was a Visiting Professor with the Department of Electrical and Computer Engineering, University of Alberta, Edmonton, AB, Canada. His research interests include power electronics for renewable generation systems, microgrids, and energy internet.